

Design and fabrication of resonator-quantum well infrared photodetector for SF₆ gas sensor application

Jason Sun
Kwong-Kit Choi
Eric DeCuir, Jr.
Kimberley Olver
Richard Fu

Design and fabrication of resonator-quantum well infrared photodetector for SF₆ gas sensor application

Jason Sun,* Kwong-Kit Choi, Eric DeCuir Jr., Kimberley Olver, and Richard Fu
U.S. Army Research Laboratory, Adelphi, Maryland, United States

Abstract. The infrared absorption of SF₆ gas is narrowband and peaks at 10.6 μm . This narrowband absorption posts a stringent requirement on the corresponding sensors as they need to collect enough signal from this limited spectral bandwidth to maintain a high sensitivity. Resonator-quantum well infrared photodetectors (R-QWIPs) are the next generation of QWIP detectors that use resonances to increase the quantum efficiency for more efficient signal collection. Since the resonant approach is applicable to narrowband as well as broadband, it is particularly suitable for this application. We designed and fabricated R-QWIPs for SF₆ gas detection. To achieve the expected performance, the detector geometry must be produced according to precise specifications. In particular, the height of the diffractive elements and the thickness of the active resonator must be uniform, and accurately realized to within 0.05 μm . Additionally, the substrates of the detectors must be completely removed to prevent the escape of unabsorbed light in the detectors. To achieve these specifications, two optimized inductively coupled plasma etching processes were developed. Due to submicron detector feature sizes and overlay tolerance, we used an advanced semiconductor material lithography stepper instead of a contact mask aligner to pattern wafers. Using these etching techniques and tool, we have fabricated focal plane arrays with 30- μm pixel pitch and 320 \times 256 format. The initial test revealed promising results. © The Authors. Published by SPIE under a Creative Commons Attribution 3.0 Unported License. Distribution or reproduction of this work in whole or in part requires full attribution of the original publication, including its DOI. [DOI: 10.1117/1.JMM.16.3.034504]

Keywords: resonance; inductively coupled plasma etching; quantum efficiency; quantum well infrared photodetector; GaAs substrate removal; advanced semiconductor material lithography stepper; SF₆ gas; focal plane array.

Paper 17029P received Mar. 21, 2017; accepted for publication Jul. 24, 2017; published online Sep. 1, 2017.

1 Introduction

A quantum well infrared photodetector (QWIP) requires an optical coupling structure to detect normal incident light. Many optical designs, especially grating coupling, have been implemented,¹⁻⁷ but with a modest quantum efficiency (QE) 5% to 10%, they are generally only suitable for applications with a long integration time.

Current commercial SF₆ gas detectors use a grating coupling structure, therefore, the QE of the detectors is less than 10%. Since this very narrow band has a limited spectral range, a larger QE is needed to achieve a high sensitivity of the detectors.

Recently, we have established a highly reliable and accurate electromagnetic (EM) model to calculate the QE of an infrared detector. We applied it to design a new detector structure, which uses a resonator to increase the QE of the detectors.⁸⁻¹⁰ We call the detector resonator-QWIP or R-QWIP. The R-QWIP structure uses the active pixel volume as a resonator to store the incident light until the light is absorbed. By designing a properly sized detector volume, the trapped light forms a constructive interference pattern, with which the internal optical intensity is greatly increased, thereby yielding a large QE even with a small active layer thickness of 1.0 μm . Thus, R-QWIP is very suitable for this 10.6 μm narrowband application.

Inductively coupled plasma (ICP) etching has distinct advantages over reactive ion etching in that the etching rates are considerably higher, the uniformity is much better,

and the sidewalls of the etched material are highly anisotropic due to the higher plasma density and lower operating pressure. Therefore, ICP etching is a promising process for pattern transfer required during microelectronic and optoelectronic fabrication. To fabricate R-QWIP focal plane arrays (FPAs) and fan-out test devices, two optimized ICP etching processes were developed. The selective etching process yielded a very high selectivity of etching GaAs over Al_{0.4}Ga_{0.6}As (>5000:1) and a fast GaAs etching rate (2700 $\text{\AA}/\text{min}$). This etched surface was perfectly smooth and mirror-like after processing. For the nonselective etching process, we optimized the gas ratio, RF and ICP powers, and operating pressure to yield a highly anisotropic etching profile (88 deg), high etching rate (5400 $\text{\AA}/\text{min}$). The etching nonuniformity is less than 3% across a 4-in. wafer. In addition to these, both processes are also highly reproducible and show no plasma damage to the detector material.¹¹⁻¹⁴ Due to micron detector feature size and submicron overlay tolerance, we employed an advanced semiconductor material lithography (ASML) stepper instead of a contact mask aligner to process the wafers, which offered much better resolution (0.5 versus 1 μm) and near perfect alignment between layers. Using these etching techniques and the stepper, we have fabricated numerous 320 \times 256, 30- μm pixel pitch R-QWIP FPAs with the required dimensions with their substrates completely removed.

2 Detector Design

The designed resonant structure for light coupling is shown in Fig. 1(a). In this design, the pixel pitch is 30 μm and the

*Address all correspondence to: Jason Sun, E-mail: jason.sun@arl.army.mil

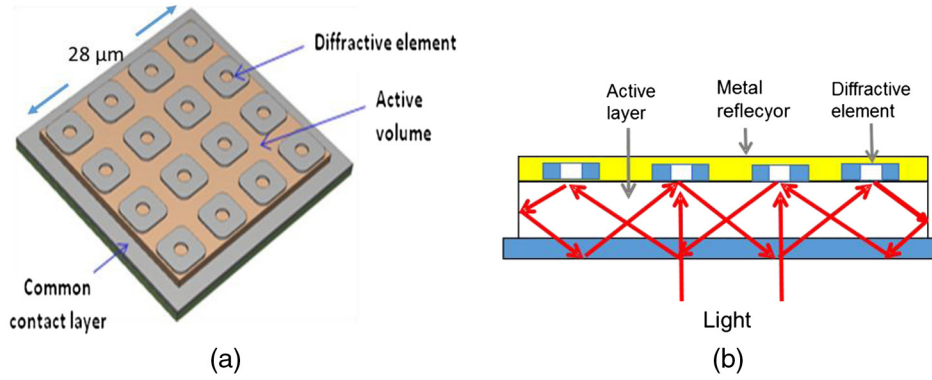


Fig. 1 (a) The optimized R-QWIP geometry for the narrowband at $10.6 \mu\text{m}$. (b) The schematic light path inside the detector.

linear pixel size is $28 \mu\text{m}$. A set of rings is fabricated into the top contact layer and then covered with gold. The detector substrate is completely removed to yield a suitable resonant detector thickness. The light is incident from the backside of the detector and is diffracted by the diffractive elements (DEs) and reflected back to the active layer as shown in Fig. 1(b) where it is trapped and circulated inside the pixel until it is absorbed eventually.

The present modeling is performed in the RF module of a commercial EM solver, COMSOL Multiphysics. The modeling procedures involve selecting the EM analysis mode, building a two-dimensional or three-dimensional detector geometry, defining constants, variables, functions, inputting subdomain properties, selecting appropriate boundary conditions, building mesh structures, setting solver parameters, performing computation, and using postprocessing to yield the required information.

To model the QE of a detector, we note that η can be expressed as⁸

$$\begin{aligned} \eta(\lambda) &= \frac{1}{P_0} \int_V dI(\mathbf{r}) = \frac{1}{P_0} \int_V \alpha(\lambda) I(\mathbf{r}, \lambda) d^3r \\ &= \frac{\alpha(\lambda)}{A \frac{c\epsilon_0}{2} E_0^2} \int_V \frac{n(\lambda)c\epsilon_0}{2} |E_z(\mathbf{r}, \lambda)|^2 d^3r \\ &= \frac{n(\lambda)\alpha(\lambda)}{AE_0^2} \int_V |E_z(\mathbf{r}, \lambda)|^2 d^3r, \end{aligned} \quad (1)$$

where P_0 is the incident power from the air, $I(r)$ is the optical intensity, A is the detector area, E_0 is the incident electric field, E_z is the electric component pointing in the z -direction, $n(\lambda)$ is the material refractive index, $\alpha(\lambda)$ is the absorption coefficient, and V is the detector active volume. Equation (1) is suitable for QWIPs with E_z polarization dependence. For the usual infrared materials with isotropic absorption coefficient, Eq. (1) is still applicable after $E_z(r)$ is replaced by the total $E(r)$.

For a given QWIP energy band structure, the detector thermal sensitivity (NE ΔT) is strongly dependent on the electron doping density (N_D) in the quantum well. For the present application of $10.6 \mu\text{m}$ detection, we can analyze the NE ΔT variation as a function of N_D through detector modeling. The QWIP material under consideration is made of 15 periods of 56 \AA GaAs/ 600 \AA Al_{0.2}Ga_{0.8}As sandwiched between a top and a bottom GaAs contact layer.

The active layer thickness (t_{ac}) is thus $1.0 \mu\text{m}$. The material is designed to detect at a peak wavelength λ_{peak} of $10.6 \mu\text{m}$ with a $1\text{-}\mu\text{m}$ bandwidth. The absorption coefficient (α) of the material with different N_D is calculated from the standard transfer matrix method^{15,16} and is shown in Fig. 2(a). The peak α varies from 0.05 to $0.25 \mu\text{m}^{-1}$ when N_D increases from 0.2 to $1.0 \times 10^{18} \text{ cm}^{-3}$. Fabricating this material into a resonator-quantum well infrared photodetector (R-QWIP) structure, its theoretical absorption QE, which is obtained from EM modeling, is shown in Fig. 2(b). It ranges from 30% to 70% for a $28\text{-}\mu\text{m}$ square detector. Assuming a typical gain (g) of 0.6 at the saturation voltage for this material structure, the corresponding conversion efficiency [CE(\equiv QE \times g)] ranges from 18% to 42%.

The background photocurrent generated by an R-QWIP can be calculated by integrating the modeled CE with the incident photon flux and the dark current can be estimated by adopting a semiempirical equation.¹⁷ With knowledge of both the photocurrent and dark current at different N_d , the variation of NE ΔT can be readily deduced. Figure 3 shows that, under a fixed integration time of 16 ms and $F/2.3$ optics, the NE ΔT varies as a function of doping density at different operating temperatures. It can be seen from these doping density-dependent NE ΔT calculations that $N_d = 0.3$ and $N_d = 0.8$ provide the lowest NE ΔT at temperatures less than or greater than 55 K, respectively.

3 Detector Fabrication

Our R-QWIP FPA and test device fabrication required five mask layers.^{18–20} For this work, we used an ASML stepper instead of a contact mask aligner to pattern all layers because of our submicron detector feature sizes and overlay tolerance. For the ASML PAS 5500 stepper, the wafer alignment marks are diffraction gratings as shown in Fig. 3(a). There are marks for both the x - and y -directions. These marks are illuminated by a HeNe laser at a single wavelength near 632.8 nm . The reflected wave exhibits a diffraction pattern of bright and dark lines that are focused on a sensor. The stage is moved slightly to learn the best position to match the sensor and that stage position is used to calculate the stage position to place the die under the center of the optical column. The wafer is moved to the lens center (or shifted by a fixed amount from center) and the die is exposed. The stage positions for the remaining dies are calculated and those dies are also exposed. Initially, the marks were patterned and etched into the starting wafer. To reduce the number of

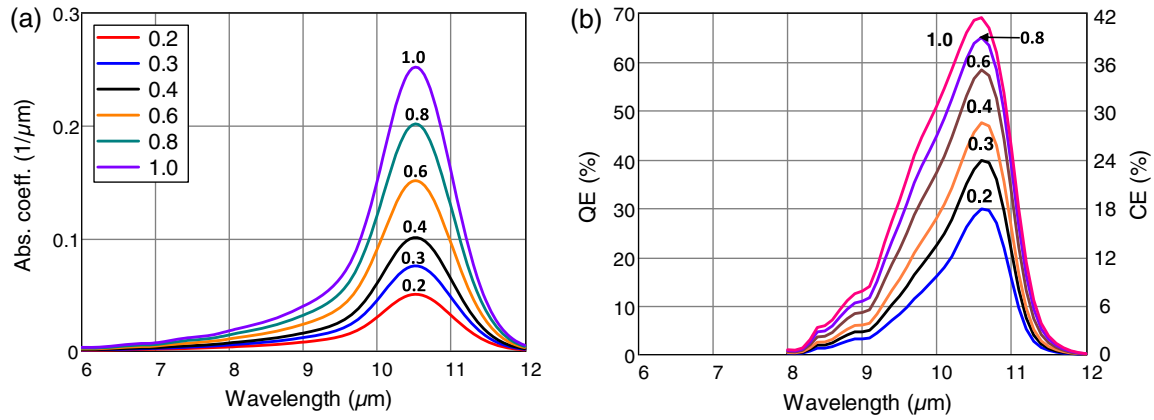


Fig. 2 (a) The designed absorption coefficient of a QWIP with different N_D (in the unit of 10^{18}cm^{-3}). (b) The corresponding modeled QE and conversion efficiency CE with $1\text{-}\mu\text{m}$ thick active material and a pixel size of $28\ \mu\text{m} \times 28\ \mu\text{m}$.

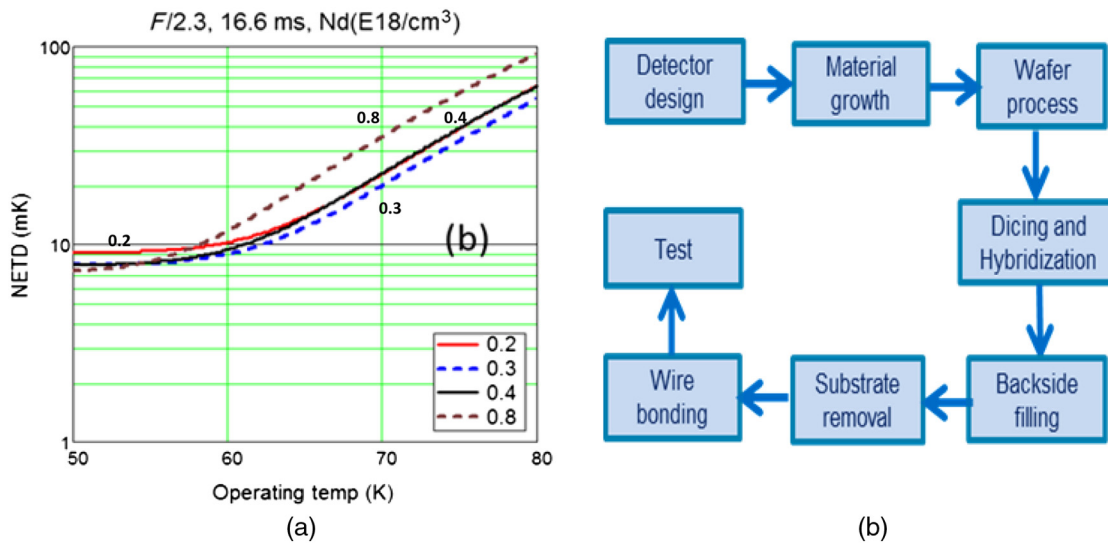


Fig. 3 (a) Modeled sensitivity (NETD) as a function of doping density (N_D) at different operating temperatures and (b) detector FPA fabrication flowchart.

operations, we combined the mark creation (0 layer) and the first layer of our device. To give maximum contrast in the diffracted pattern, the etch depth is set at $\lambda/4n$, which resulted in an optical path difference of π , where λ is the wavelength of the laser light and n is the index of refraction of the material above the marks (usually photoresist or oxide). This etch depth calculation of the mark gave a value approximately equal to $632.8/4/1.45 = 110\ \text{nm}$ ($1100\ \text{\AA}$). However, our first detector layer etching depth needed to be $\sim 4500\ \text{\AA}$. Therefore, a concern was to ensure that the system could recognize the $4500\text{-}\text{\AA}$ depth marks and perform the overlay alignment correctly. In this regard, a dummy GaAs wafer was tested beforehand to minimize the loss of expensive detector wafers. During this testing, we verified that the system could identify the $4500\text{-}\text{\AA}$ depth marks and perform precise alignments for all steps with various types and thicknesses of photoresist that would be used during the detector fabrication.

For the first layer of the FPAs, we created an array of rings as the DEs on wafers to scatter normal incident light into the detector. R-QWIP structure uses the active pixel volume as a

resonator to store the incident light until the light is absorbed. We coated a $1.4\text{-}\mu\text{m}$ -thick AZ5214 photoresist on the wafer using an EVG 120 resist processing cluster. The resist was baked at 110°C for 1 min in the system. The DEs were formed by using our optimized selective ICP etching process to etch down to the $15\text{-}\text{\AA}$ top etching stop layer. The etching depth is 4000 to $5000\ \text{\AA}$. Since our selective etching process has a very high selectivity of etching GaAs over AlGaAs (greater than $5000:1$ for $\text{Al}_{0.4}\text{Ga}_{0.6}\text{As}$), a $15\text{-}\text{\AA}$ thick stop etching layer is sufficient to define the DE height. Figure 4(b) shows a microscope picture of the dies after first selective ICP etching. The etching is uniform, and the etching surface is clean and smooth. The second masking step defines the ground contact area located outside the pixel area. Our nonselective ICP etching recipe was used to reach the common ground contact layer. The optimized etching process uses a finite RF power, which is necessary to create a vertical sidewall, and a low-gas pressure to give a uniform etching across the wafer. We used the third mask to define the lift-off areas for the deposition of Pd ($50\ \text{\AA}$)/Ge ($200\ \text{\AA}$)/Au ($300\ \text{\AA}$)/Pd ($50\ \text{\AA}$)/Au ($5000\ \text{\AA}$) metal and

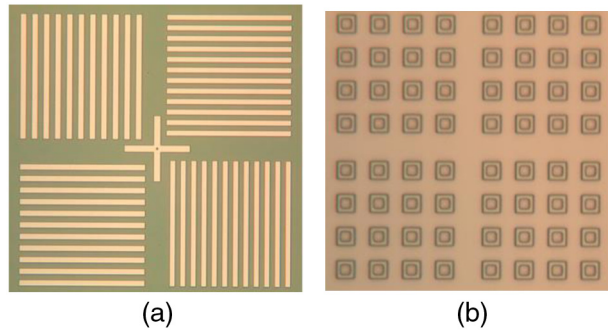


Fig. 4 Two microscope pictures taken after first combined layer ICP etching (a) stepper alignment mark and (b) fabricated detector DEs (320×256 format and $30\text{-}\mu\text{m}$ pixel pitch size). It contains four detector pixels and each pixel pitch is $30\ \mu\text{m}$.

it was followed by a furnace annealing at 350°C for 25 min. With the help of DEs, we can use a positive photoresist (PR) instead of a negative PR or an image reversal to pattern the wafer. DEs are used to convert the normal incident UV light to horizontal through diffraction, which can create a PR undercut for metal lift off. Figure 5(a) shows a picture taken after metal lift off.

We used the fourth mask to define the pixels. We opened the pixel areas while other areas were covered with photoresist. In the pixel areas, the metal squares were used as etching masks and nonselective ICP etching was utilized to create individual pixels. The fifth mask is an indium bump mask. We coated $9\text{-}\mu\text{m}$ -thick PR (AZ9245) and deposited $6\text{-}\mu\text{m}$ -tall indium bumps on the wafer using a thermal evaporator. Figure 5(b) shows a microscope picture taken after indium bump deposition. Figure 3(b) shows a detail process flowchart. After we finished the wafer process, the wafers were diced into FPAs and test devices. Each test structure contains 33×33 pixels connected in parallel. The candidate FPAs and test devices were hybridized to readout integrated circuits (ROIC) and fan-outs. Low viscosity epoxy under-fill was used to fill voids between the ROIC and FPA material for mechanical stability during the final substrate removal process. Previous studies have shown that thinned QWIP FPAs offer several advantages over unthinned FPAs.¹⁴ In regards to the R-QWIP structure, substrate removal is specifically required for intended operation. The thinned R-QWIP FPAs enhance the resonant effects, and the QE can increase by a factor of 3 to 4 according to EM

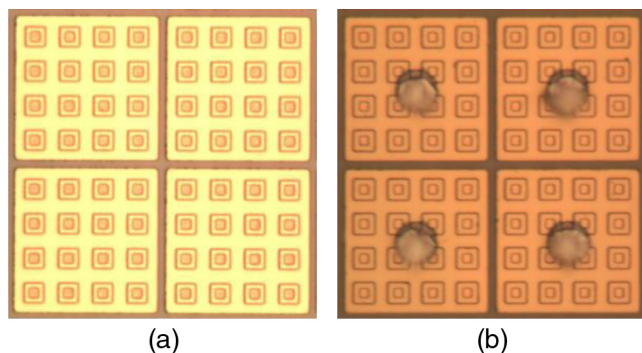


Fig. 5 Two microscope pictures taken after (a) metallization and (b) indium bump deposition. Both pictures contain four detector pixels and each pixel pitch is $30\ \mu\text{m}$.

modeling. To totally remove the FPA's substrate, we first mechanically lapped the substrate within $50\ \mu\text{m}$ and then final removal was achieved with a Unaxis VLR 700 Etch System ($\sim 2\text{-h}$ plasma etch). After this last substrate etch, the surface of the die was uniform, smooth, and mirror-like.

4 Detector Characteristic

To obtain the lowest NE ΔT within an allowed τ_{int} at the highest T , we chose small N_{D} of $0.2 \times 10^{18}\ \text{cm}^{-3}$ (labeled as Det. A) and $0.3 \times 10^{18}\ \text{cm}^{-3}$ (labeled as Det. B) according to the above calculation. Their QE was modeled and the result is 30% for Det. A and 40% for Det. B as shown in Fig. 1(b). In Figs. 6 and 7, we plot the experimental CE and QE measured at $T = 10\ \text{K}$ for Det. A and Det. B, respectively. Both detectors have a similar detection spectrum, which is peaked at $10.2\ \mu\text{m}$. Det. A has a maximum CE of 20.2% and a QE of 29.4% at $V = 2.5\ \text{V}$. These measured values are in excellent agreement with the theoretical values of 18% and 30%, respectively. However, Det. B, which has a higher N_{D} , is measured with a CE of 15.0% and a QE of 26.3%, which is lower than their expected values of 24% and 40%, respectively.

To yield a better understanding of the discrepancy, we compared the spectral response of the R-QWIPs at $2.5\ \text{V}$ with the α spectrum in Fig. 8. These material intrinsic absorption spectra were characterized at $0.6\ \text{V}$ substrate voltage and $77\ \text{K}$ operating temperature. In this plot, the detection spectrum of the R-QWIP is clearly displaced from the material absorption spectrum. This displacement is mainly caused by the resonant wavelength λ_{res} of the R-QWIPs being at $10.2\ \mu\text{m}$ instead of the targeted λ_{peak} of $10.6\ \mu\text{m}$. The shorter λ_{res} indicates that the material refractive index n is slightly smaller than the assumed $n = 3.0$ in the modeling for this material composition in this wavelength range. The displacement is larger for Det. B because the material absorbs at a slightly longer wavelength and it is peaked at $10.7\ \mu\text{m}$ as seen in Fig. 7.

To yield a more definitive conclusion, we fitted the detector QE using n as a fitting parameter and the modeling is based on the observed α spectrum and the fabricated ring pattern in Fig. 3(b). The result is shown in Fig. 9 for $n = 2.85$. With the new n , the modeled QEs are now peaked at $10.2\ \mu\text{m}$. It underestimated the experimental QE value by 18% for Det. A while it overestimated Det. B by 10%. The modeling also gives narrower lineshapes. We attribute these narrower lineshapes to the adopted α spectrum, which was measured at $0.6\ \text{V}$ instead of $2.5\ \text{V}$. As seen in Figs. 5 and 6, there is substantial spectral broadening at the higher bias that may indicate the broadening of the intrinsic α . The overall agreement is thus satisfactory given the anticipated differences due to bias. From this analysis, it should be possible to shift λ_{res} to $10.6\ \mu\text{m}$ by adjusting the ring pattern using $n = 2.85$ and to subsequently obtain a larger QE for both detectors.

In the present experiment, we adopted the Indigo ISC 9705 ROICs with a well capacity of $18\ \text{Me}^-$ and pixel pitch of $30\ \mu\text{m}$. Using the directly measured I_{p} and I_{d} , NE ΔT at τ_{int} of 2 ms and $F/2$ optics is shown in Fig. 10 for Det. A at $T = 55\ \text{K}$ and Det. B at $T = 60\ \text{K}$. Setting N_{tot} at $9\ \text{Me}^-$ for the present ROIC, one is able to operate the FPAs at a small bias of $0.5\ \text{V}$ for this τ_{int} , in which photoconductive (PC) g is 0.31 for Det. A and 0.35 for Det. B.

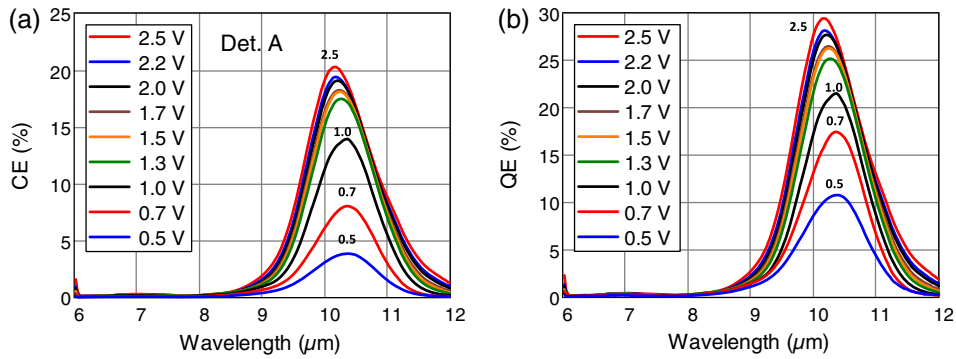


Fig. 6 (a) The measured CE and (b) the deduced QE of Det. A.

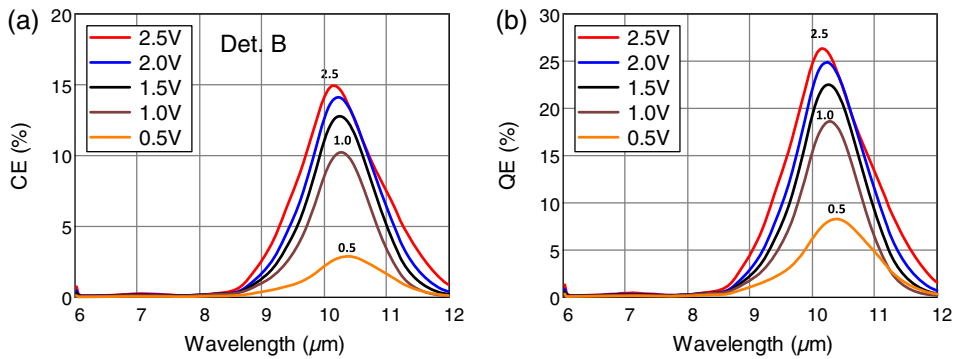


Fig. 7 (a) The measured CE and (b) the deduced QE of Det. B.

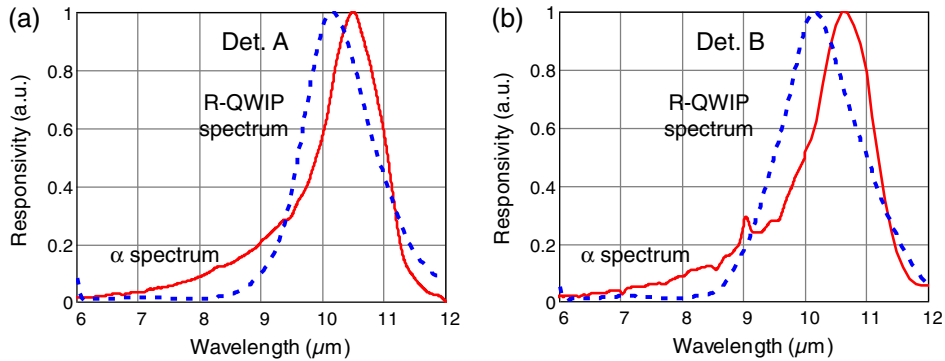


Fig. 8 The comparison between the spectral response of R-QWIP and LAD for (a) Det. A and (b) Det. B.

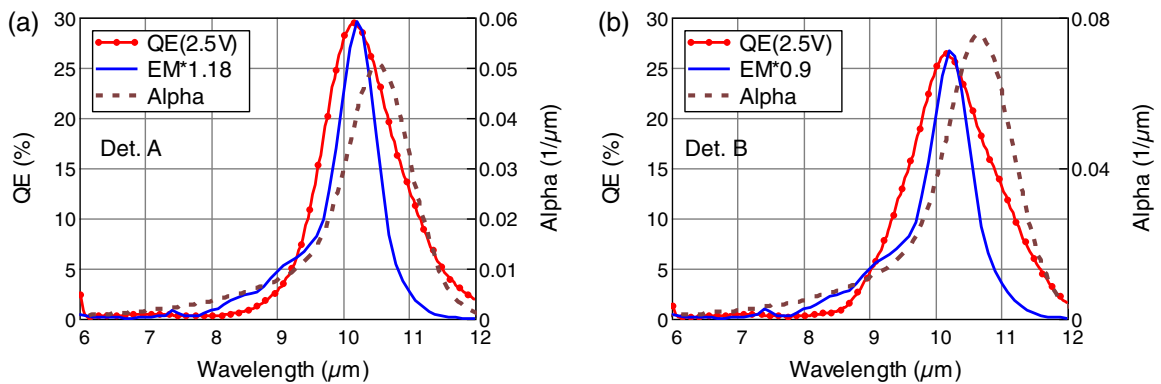


Fig. 9 The experimental α lineshape at 0.6 V (dashed curve), the experimental QE at 2.5 V (solid curve with cycles), and the modeled QE (solid curve) for (a) Det. A and (b) Det. B.

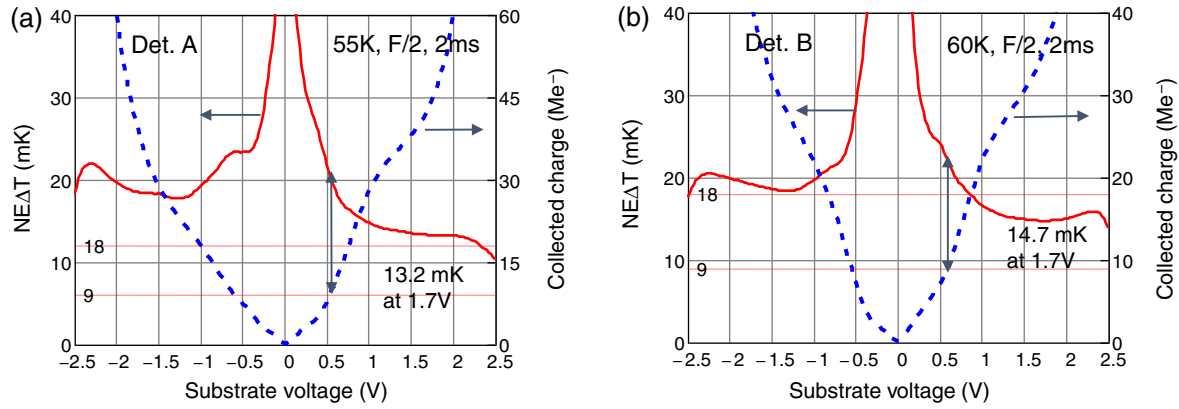


Fig. 10 The calculated $NE\Delta T$ and N_{tot} of FPAs made from Det. A and Det. B. They are based on the measured I_d/I_p ratio at a fixed τ_{int} of 2 ms under $F/2$ optics. Notice the difference in the operating temperature.

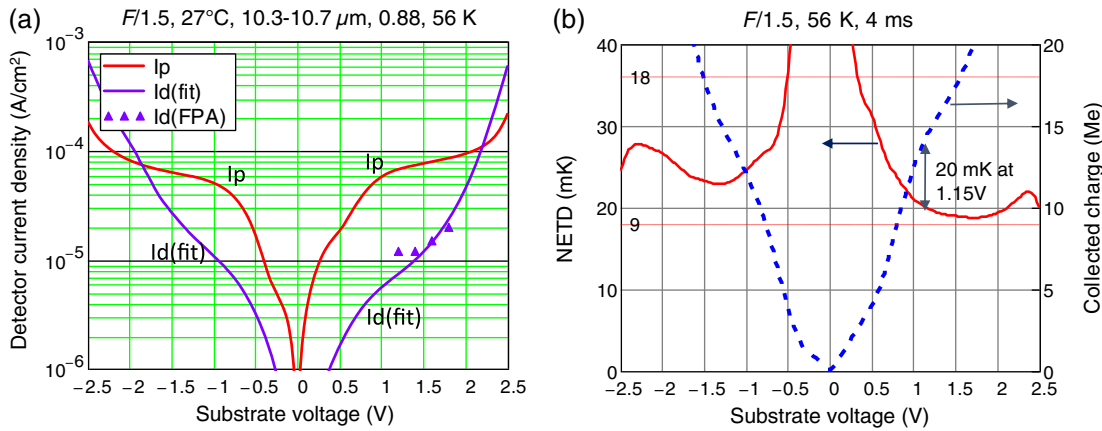


Fig. 11 (a) The calculated I_p of Det. B based on the measured CE spectrum and the fitted FPA I_d at 56 K. (b) The calculated $NE\Delta T$ and N_{tot} of the FPA at a fixed τ_{int} of 4 ms under $F/1.5$ optics.

With these smaller PC gains, both FPAs were able to offer a small $NE\Delta T$ of 20 mK. Shorter τ_{int} was possible at higher bias albeit with a higher $NE\Delta T$ because of a larger g . Therefore, the present low N_D materials are the proper choices for this operating condition. We should also note that if the ROIC's N_c is larger, the FPAs should be able to operate at a higher bias such as 1.7 V, in which $NE\Delta T$ is 14 mK for $\tau_{int} = 2$ ms and $N_{tot} = 35$ to 40 Me^- .

On the other hand, if the FPAs are operated under a more challenging condition where the detection wavelength range is reduced, a longer τ_{int} must be employed. For example, for SF_6 gas detection, it requires the detection of a filtered photon flux between 10.3 and 10.7 μm . Assuming the optical transmission of the filter is 0.88, I_p will be reduced by 3.34 times even with a faster optics of $F/1.5$. Figure 11(a) shows the calculated I_p of Det. B according to the CE spectrum within this wavelength range. With the fitted FPA I_d at $T = 56$ K, one will need to increase the bias to 1.15 V shown in Fig. 11(b) to achieve the same $NE\Delta T$ of 20 mK at $\tau_{int} = 4$ ms and $N_{tot} = 14$ Me^- . Therefore, under this more severe operating condition, a higher N_D may be beneficial in reducing either τ_{int} for the same $NE\Delta T$ or vice versa. Nevertheless, in case the theoretical QE of 40% of Det. B can be realized using a more suitable resonant design, the shorter τ_{int} of 2 ms

could be recovered. It is then an open question on whether a higher doping is more suitable for this application.

5 Conclusion

In this work, we have applied R-QWIPs to narrowband 10.6 μm detection for SF_6 gas sensor application. To fabricate R-QWIP FPAs and test devices, two optimized ICP etching processes were developed and an ASML stepper was used to fabricate R-QWIP FPAs with the design dimensions and required etching depths. The substrates of the FPAs and test devices were completely removed to enhance the resonant effects. With only a 1- μm -thick active layer and low doping densities of 0.2 and 0.3×10^{18} cm^{-3} , a QE of 30% and 26% has been achieved, respectively. These detectors cutoff at 11 μm and reach high sensitivities approaching 20 mK with a half-well capacity of 9 Me^- when they are operated with $F/2$ optics at 60 K and using a 2-ms integration time. Higher sensitivity is expected at higher bias and larger well capacity. For the more demanding SF_6 gas sensing, the present FPA should reach the same sensitivity with $F/1.5$ optics at 56 K and using a 4-ms integration time. It is anticipated that further optimized resonant structures with higher sensitivity at the wavelengths of interest could further reduce the integration time.

Acknowledgments

The authors would like to thank the support of FPA processing, testing, and demonstration at the FLIR system and the U.S. National Institute of Standards and Technology (NIST).

References

1. J. Y. Andersson and L. Lundqvist, "Grating-coupled quantum-well infrared detectors: theory and performance," *J. Appl. Phys.* **71**, 3600–3610 (1992).
2. B. Brill and G. Sarusi, "System considerations in the design of QWIP-based thermal imagers," *Proc. SPIE* **3436**, 270 (1998).
3. T. R. Schimert et al., "Enhanced quantum well infrared photodetector with novel multiple quantum well grating structure," *Appl. Phys. Lett.* **68**, 2846–2848 (1996).
4. K. K. Choi et al., "Quantum grid infrared spectrometer," *Appl. Phys. Lett.* **84**, 4439–4441 (2004).
5. C. J. Chen et al., "Corrugated quantum well infrared photodetectors for normal incident light coupling," *Appl. Phys. Lett.* **68**, 1446–1448 (1996).
6. W. Wu, A. Bonakdar, and H. Mosheni, "Plasmonic enhanced quantum well infrared photodetector with high detectivity," *Appl. Phys. Lett.* **96**, 161107 (2010).
7. S. Kalchmair et al., "Photonic crystal slab quantum well infrared photodetector," *Appl. Phys. Lett.* **98**, 011105 (2011).
8. K. K. Choi et al., "Electromagnetic modeling and design of quantum well infrared photodetectors," *IEEE J. Sel. Top. Quantum Electron.* **19**, 3800310 (2013).
9. K. K. Choi et al., "Resonator-quantum well infrared photodetectors," *Appl. Phys. Lett.* **103**, 201113 (2013).
10. K. K. Choi et al., "Electromagnetic modeling and resonant detectors and arrays," *Infrared Phys. Technol.* **70**, 153–161 (2014).
11. J. Sun et al., "Fabrication of pyramidal corrugated quantum well infrared photodetector focal plane arrays by inductively coupled plasma etching with BCl₃/Ar," *J. Micro/Nanolithogr. MEMS MOEMS* **11**, 043003 (2012).
12. A. Mitchell et al., "Real-time, in situ monitoring of GaAs and AlGaAs photoluminescence during plasma processing," *Appl. Phys. Lett.* **56**(9), 821–823 (1990).
13. C. M. Knoedler, L. Osterling, and H. Shtikman, "Reactive ion etching damage to GaAs layers with etch stops," *J. Vac. Sci. Technol.* **B6**, 1573 (1988).
14. S. J. Pearton et al., "Reactive ion etching of GaAs with CCl₂F₂:O₂: etch rates, surface chemistry, and residual damage," *J. Appl. Phys.* **65**, 1281–1292 (1989).
15. K. K. Choi et al., "Detection wavelength of InGaAs/AlGaAs quantum wells and superlattices," *J. Appl. Phys.* **91**, 551–564 (2002).
16. K. K. Choi et al., "Electromagnetic modeling of QWIP FPA pixels," *Proc. SPIE* **8012**, 80120R (2011).
17. K. K. Choi et al., "C-QWIP focal plane arrays," *Inf. Phys. Technol.* **52**, 364–370 (2009).
18. J. Sun, K. K. Choi, and K. Olver, "Fabrication of resonator-quantum well infrared photodetector test devices," *J. Micro/Nanolithogr. MEMS MOEMS* **13**, 013004 (2014).
19. J. Sun et al., "Advanced inductively coupled plasma etching processes for fabrication of resonator-quantum well infrared photodetector," *Infrared Phys. Technol.* **70**, 25–29 (2015).
20. J. Sun et al., "Advanced substrate thinning process for GaAs-based devices," *J. Micro/Nanolith. MEMS MOEMS* **10**, 023004 (2011).

Jason Sun is a physicist at the U.S. Army Research Laboratory, Adelphi, Maryland, USA. He has experiences in a wide range of optoelectronic and RF device physics and fabrication. He has many years of experience in research on conventional and high-T_c superconductors and expertise in high-critical temperature (T_c) superconductor epitaxial thin film growth and characteristics. His current interest is QWIP FPA research and fabrication.

Kwong-Kit Choi received his PhD in physics from Yale University in 1984. He is currently a senior research scientist for physical sciences at the Army Research Lab. His interest spans from basic physics to focal plane array demonstration.

Eric DeCuir Jr. received his MS and PhD degrees in microelectronics and photonics from the University of Arkansas in 2005 and 2008, respectively. His research portfolio includes more than 10 years of experience with both growth and electrical/optical characterization of III-nitride, III-V, and II-VI semiconductor materials. This work has focused on optoelectronic devices and investigating both bulk and quantum confined properties of superlattices, quantum wells, quantum wires, and quantum dot structures.

Kimberley Olver received her BA degree in chemistry from Goucher College in 1981. She is currently working as a physical scientist at the U.S. Army Research Laboratory. Her main interests are processing and characterization of both II-VI and III-V material systems. Prior to joining ARL, she was employed as a senior engineer at Lockheed Martin Corporation in the Advanced Infrared Technology Group. Her work included IR focal plane array packaging and array characterization.

Richard Fu received his PhD in materials science from the State University of New York at Buffalo in 1998. He is currently a research scientist at U.S. Army Research Laboratory (ARL) and was a lead scientist in industry R&D for 10 years prior to joining ARL in 2006. His research focuses on nano/thin film and infrared materials, fabrications, and their applications in sensors and electron devices.